International Journal of Mechanical, Industrial and Aerospace Sciences
ISSN: 2517-9950
Vol:9, No:4, 2015

CFD Modeling of Boiling in a Microchannel Based On Phase-Field Method

Rahim Jafari, Tuba Okutucu-Özyurt

***Abstract*—**The hydrodynamics and heat transfer characteristics of a vaporized elongated bubble in a rectangular microchannel have been simulated based on Cahn-Hilliard phase-field method. In the simulations, the initially nucleated bubble starts growing as it comes in contact with superheated water. The growing shape of the bubble compared well with the available experimental data in the literature.

***Keywords*—**Microchannel, boiling, Cahn-Hilliard method, Two-phase flow, Simulation.

I. Introduction

FLOW boiling through microchannels has been extensively studied as a cooling alternative for microelectronic devices because of its capability of providing a high heat transfer rate. Vaporized bubble of microscopic size in a microchannel grows rapidly and fills the entire cross section of the microchannel in milliseconds, and eventually, an elongated bubble or slug flow appears in the microchannel. Moreover, at the microscale, the surface tension and evaporation momentum forces are the dominant forces controlling the bubble dynamics [1]. Dong et al. [2] investigated the effect of bubble nucleation, growth and departure on fluid flow and heat transfer in a microchannel via lattice Boltzman 2-D modeling. A single seed bubble, a cavity, two cavities, one seed bubble and a reentrant cavity were simulated in a microchannel with dimensions of 0.2mm×5.3mm.

Sun et al. [3] proposed a vapor-liquid phase model in ANSYS FLUENT which considers both superheated and saturated phases. The vapor near the wall gets heated and becomes superheated, which drives the mass transfer at the interface. The vapor stays motionless while the saturated liquid and the interface are driven away from the wall. Magnini et al. [4] implemented ANSYS FLUENT to investigate in detail the bubble dynamics and the wall heat transfer of flow boiling in a circular microchannel of diameter 0.5 mm in 2-D axisymmetrical formulation. Different refrigerants, namely, R113, R134a and R245fa were investigated with two different saturation temperatures of 31°C and 50°C. The bubble nose acceleration to downstream was in good agreement with a theoretical model [5].

R. J. is a PhD. Candidate in the Department of Mechanical Engineering, Middle East Technical University, Dumlupınar Bulvarı, No:1, 06800, Çankaya, Ankara, Turkey (Corresponding author; phone: 534 299 3004; e-mail: e170530@metu.edu.tr)

T. O. is an Associate Professor in the Department of Mechanical Engineering, Middle East Technical University, Dumlupınar Bulvarı, No:1, 06800, Çankaya, Ankara, Turkey (phone: 312 210 2575; e-mail: okutucu@metu.edu.tr)

Mukherjee et al. [6] studied a vapor bubble growing on a heated wall inside a microchannel with a hydraulic diameter of 229 μm. They solved the continuity, Navier- Stokes and energy equations using the SIMPLER algorithm. Firstly, the water bubble growth rate and the bubble shape were validated by experimental results. Then a parametric numerical study was carried out to analyze the effects of the wall superheat, the inlet liquid flow rate, the surface tension and the contact angle on the bubble growth rate inside the microchannel. The aim of study is to employ the phase-field model to investigate the hydrodynamics and heat transfer characteristics of two-phase flow during nucleate boiling in microchannels.

II. Phase-Field Method

The interface of two immiscible fluids often needs special consideration. One method of handling moving boundaries is to keep track of the motion of material points residing on the interface. Numerically, this may be realized by using grid points moving either with the local fluid velocity or a mesh velocity. This Lagrangian approach is often known as interface tracking. However, interfacial deformation causes some difficulties as remeshing and interpolation increasing the computational cost and error. An alternative to interface tracking is to track the fluid flow of both components on a fixed Eulerian grid, with the interface being determined or reconstructed at each time step by using a scalar indicator function. Examples of this class of methods are the volume of fluid (VOF) method, the level-set method (LS) and the phase-field method [7]. The diffuse interface models for a wide variety of interfacial phenomena such as binary fluids are addressed in literature [8]-[10]. The interface topology is estimated poorly by the volume of fluid approach used to calculate the surface tension force [11]. The phase-field method not only convects the fluid interface as in the level set method, but it also ensures that the total energy of the system diminishes correctly.

The phase-field based models replace sharp fluid-material interfaces by thin but nonzero thickness transition regions in which the interfacial forces are smoothly distributed [12]. The phase-field method has been broadly used in physics, material science [13], fracture mechanics [14] and multiphase flow [15], [16]. The basic idea is to introduce an order parameter or phase-field that varies continuously over thin interfacial layers and is mostly uniform in the bulk phases. The order parameter has a physical meaning, and can be applied to different phase change phenomena by a proper modification of the free energy. An extremely thin interface layer is required to properly model the physics of the problem. In addition,

relatively high computational resolution is required to handle the large gradients at the interface [17].

The interface has a small but finite thickness which contains two mixed components (phases), and stores a mixing energy. The free energy density of an isothermal mixture of two immiscible fluids is the sum of the mixing energy and the elastic energy. The mixing energy may be expressed as [10]

$$f_{mix}(\emptyset, \nabla\emptyset) = \frac{1}{2}\lambda|\nabla\emptyset|^2 + \frac{\lambda}{4\epsilon^2}(\emptyset^2 - 1)^2 \quad (1)$$

where ϕ is the dimensionless phase-field variable defined such that the volume fraction of the components of the fluid are $(1+\phi)/2$ and $(1-\phi)/2$. The quantity λ [N] is the mixing energy density, and ϵ [m] is a capillary width that scales with the thickness of the interface.

The evolution of the phase-field variable ϕ is governed by the Cahn-Hilliard equation, which is a 4th-order partial differential equation in the form

$$\frac{\partial\phi}{\partial t} + u \cdot \nabla\phi = \nabla \cdot \gamma\nabla G \quad (2)$$

where u and γ are the velocity vector [m/s] and the mobility [m3·s/kg], respectively, and G [Pa] is the chemical potential which is defined as

$$G = \lambda\left[-\nabla^2\phi + \frac{\phi(\phi^2-1)}{\epsilon^2}\right] \quad (3)$$

The mixing energy density, λ, and the capillary width, ϵ, are related to the surface tension coefficient, σ [N/m], through (4) [10]

$$\sigma = \frac{2\sqrt{2}}{3}\frac{\lambda}{\epsilon} \quad (4)$$

The interface thickness is assumed to be the half of the mesh element size at the interface. Then the capillary width, and consequently, the mixing energy density may be found using (4). For instance, if the mesh size at the interface is 0.8 μm, the capillary width will be $\epsilon = 0.4$ μm and for water with a surface tension of σ = 0.0588 N/m, the mixing energy density will be λ = 0.25×10-6 N.

The Cahn-Hilliard equation forces ϕ to take a value of 1 or −1 except in a very thin region at the fluid-fluid interface.

The phase-field interface decomposes (2) into two second-order partial differential equations as

$$\frac{\partial\phi}{\partial t} + u \cdot \nabla\phi = \nabla \cdot \frac{\gamma\lambda}{\epsilon^2}\nabla\psi \quad (5)$$

$$\psi = -\nabla \cdot \epsilon^2\nabla\phi + (\phi^2 - 1)\phi \quad (6)$$

where ψ is the phase-field help variable.

III. Numerical Model

It is possible to investigate the evolution of the interface as well as the bulk fluid by coupling the phase-field to the conservation laws for mass, momentum and energy. For this reason, the use of any special algorithm for tracking the interface or satisfying sharp interface balances is not required. The Cahn-Hilliard (2) for the phase-field variable is modified to include the phase change as

$$\frac{\partial\phi}{\partial t} + u \cdot \nabla\phi - \dot{m}\delta\left(\frac{V_{f,V}}{\rho_V} + \frac{V_{f,L}}{\rho_L}\right) = \nabla \cdot \frac{\gamma\lambda}{\epsilon^2}\nabla\psi \quad (7)$$

where $V_{f,L}$ and $V_{f,V}$ are the volume fractions of the liquid and the vapor, respectively.

The quantity δ [1/m] is a smoothed representation of the interface between the two phases. It is defined as

$$\delta = 6V_{f,L}(1 - V_{f,L})\frac{|\nabla\phi|}{2} \quad (8)$$

The momentum equation includes the surface tension force as a volumetric body force as

$$\rho\frac{\partial u}{\partial t} + \rho(u \cdot \nabla)u = \nabla \cdot [-pI + \mu(\nabla u + (\nabla u)^T)] + \rho g + G\nabla\phi \quad (9)$$

The continuity equation is also modified to include the effect of the phase change from liquid to vapor [18]

$$\nabla \cdot u = \dot{m}\delta\left(\frac{1}{\rho_V} - \frac{1}{\rho_L}\right) \quad (10)$$

The mass flux leaving the interface can be evaluated from the conductive heat flux as

$$\dot{m} = -\frac{k_V\nabla T}{h_{lg}} \quad (11)$$

Due to the large differences in the thermophysical properties across the interface, a more suitable correlation for the evaporation rate may be of the form

$$\dot{m} = rV_{f,L}\rho_L\frac{T - T_{sat}}{T_{sat}} \quad (12)$$

where r is a constant which is set equal to 0.1 by [19]. In the present study, $V_{f,L}$ is included in (10) for δ, and the evaporation mass flux is calculated as

$$\dot{m} = R\rho_L\frac{T - T_{sat}}{T_{sat}} \quad (13)$$

where R [m/s] is a constant , and is set to 0.1 m/s.

The mass flux appears in the energy equation as

$$\rho C_P\frac{\partial T}{\partial t} + \rho C_P(u \cdot \nabla)T = \nabla \cdot k\nabla T - \dot{m}\delta h_{lg} \quad (14)$$

where h_{lg} [J/kg] is the latent heat. The thermal conductivity and the specific heat are calculated as functions of the volume fraction of the two phases as follows

$$k = (k_L - k_V)V_{f,L} + k_V \quad (15)$$

$$C_p = (C_{p,L} - C_{p,V})V_{f,L} + C_{p,V} \quad (16)$$

IV. Geometry and Computational Domain

The growing rate and the shape of the vapor bubble inside the microchannel have been validated by the experimental data of [6] for a microchannel of 229 μm hydraulic diameter. The temperatures of the side walls and the bottom wall are set to 102.1°C. The top wall is adiabatic. Water flows through the microchannel with Reynolds number Re = 100 at saturation temperature. The contact angle at the walls is θ = 30°. Initially it is presumed that a nucleated bubble of 40 μm diameter exists inside the microchannel on the bottom wall with its center located at x = 0, y = 229 μm, and z = 20 μm as shown in Fig. 1. The simulations have been performed by using finite element software, COMSOL MultiphysicsTM.

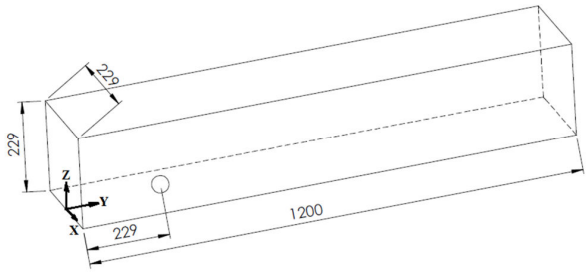

Fig. 1 The computational domain (the unit of the dimensions is μm)

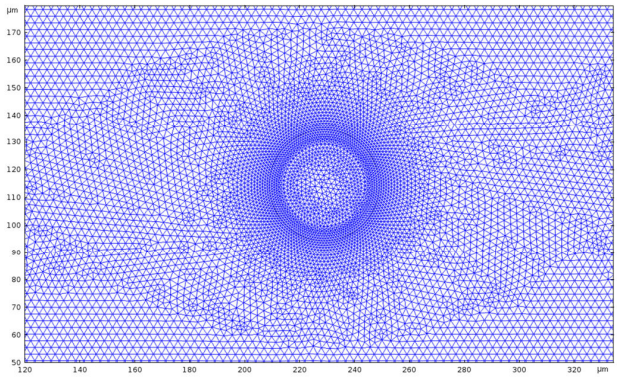

Fig. 2 The close up view of the computational mesh inside and around the nucleated bubble

At the thin interface, high gradients of the investigated parameters exist. For this reason, finer grids are required at the interface compared to the remaining regions of the model. Fig. 2 shows the distribution of the grids inside and around the bubble for the initialization of the simulations. The interface thickness is adjusted as half of the mesh element size in the region where the interface passes. Different triangular mesh sizes are used to calculate the bubble growth rate for the optimization of the numerical accuracy and the computational time. With an Intel® Xeon® CPU E5-16200 @ 3.60 GHz processor with 32 GB RAM, the computation times were about 40, 681 and 7326 minutes, for 18682, 88814 and 355256 meshes, respectively. With the two finer meshes, about 0.07 ms time difference occurred for the bubble to grow to a diameter of 0.2 mm, and a maximum difference of 4.2% has been observed between the bubble diameters obtained at the same instant. The difference in bubble diameter has reached 26.4% for the two coarser meshes. Hence, the simulations have been continued with 88814 meshes. At the interface between the liquid and vapor domains, the mesh sizes vary between 0.03 μm to 1 μm. It grows up to 2.9 μm far from the interface.

V. Results and Discussion

The simulations were performed in a two dimensional (2D) domain to save computational power and time. The gravitational force is employed along the side plane (in z-direction). The temporal evolution of the bubble shape is compared with the same experimental study [6] as illustrated in Fig. 3.

For analyzing the local hydrodynamics and heat transfer of the vapor bubble inside the microchannel in detail, the water inlet and initial temperatures and the wall temperature are set to 102.1°C. This way, the effect of convective heat transfer between the wall and water has been eliminated. Only the boiling heat transfer effect is maintained. Figs. 4 (a), (b) depict the velocity distribution inside and around the elongated bubble in the central horizontal XY plane and the central vertical ZY plane, respectively. Both distributions were captured at time t = 1.8 ms.

Fig. 4 (a) shows that the downstream velocity increases up to 0.54 m/s whereas the upstream velocity remains low at about 0.13 m/s. It may be inferred that the liquid is pushed forward at a faster rate downstream due to the bubble growth. The high rate of evaporation at the nose of the bubble, which is indicated by the greater velocities around the interface, accelerates the bubble nose movement. As a result, and based on the conservation of mass, the velocity of the vapor inside the bubble increases up to 0.8 m/s near the nose. It can also be observed that the thin liquid film between the wetted walls and the bubble downstream has higher velocity which increases the rate of evaporation.

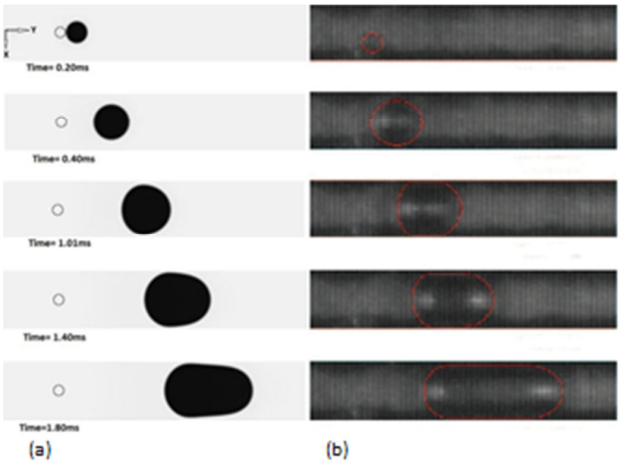

Fig. 3 The comparison of the bubble shapes of (a) the present numerical study and (b) the experimental study [6], at the same instant

Fig. 4 (b) illustrates higher velocity downstream compared to the upstream of the bubble. The downstream velocity is 0.58 m/s while the upstream velocity is about 0.13 m/s. A high rate of evaporation is indicated in the regions of high velocity gradients, namely, the bubble nose, and the liquid film between the bottom wall and the bubble nose. Since the top wall is adiabatic, there is no heat flux from the top wall into to the microchannel. Hence, the evaporation rate at the top of the bubble is lower.

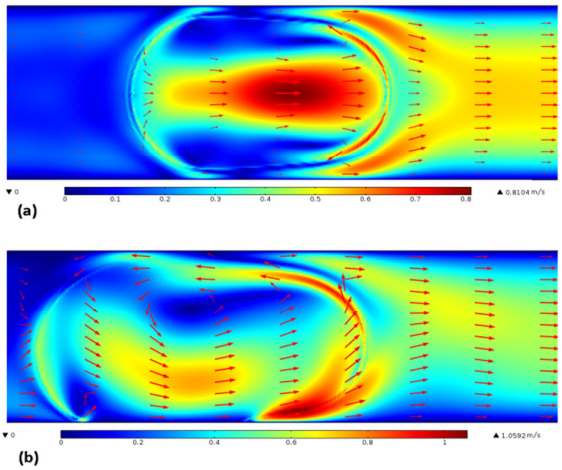

Fig. 4 The velocity distribution inside and around the elongated vapor bubble (a) XY plane and (b) ZY plane at t = 1.8 ms

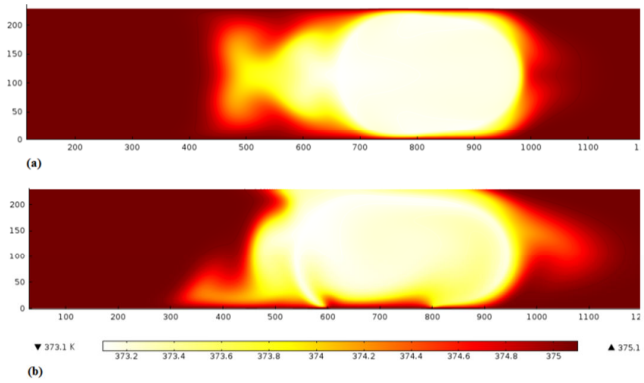

Fig. 5 The temperature distribution inside and around the elongated vapor bubble (a) XY plane and (b) ZY plane at t = 1.8 ms

Fig. 5 illustrates the temperature distribution inside and around the elongated vapor bubble in the central horizontal XY plane and the central vertical ZY plane, respectively. Fig. 5 (a) shows that the temperature inside the bubble remains at the saturation temperature due to the thin saturated liquid film between the bubble and the side walls. As the bubble evolves into an elongated one, the temperature gradient increases in the thermal boundary layer developed on the side walls. This increases the local heat flux as well. Fig. 5 (b) indicates that the adiabatic top wall remains at the saturation temperature where it meets the elongated vapor bubble. On the other hand, the part of the bubble touching the bottom wall is at the superheated temperature.

Figs. 6 (a), (b) display the pressure inside and around the elongated vapor bubble at the central XY and ZY planes. The pressure inside the bubble is 101.95 kPa which is about 450 Pa higher than that of the liquid around it. The mass flux leaving the liquid surface leads to the increase in the vapor pressure, and to the expansion of the vapor region. The difference between the downstream and upstream pressures is about 100 Pa. At the interface, especially around the nose of the bubble, higher pressure gradients exist, which is a similar trend to that observed in the velocity plots of Fig. 4. The presence of the surface tension force leads to this discontinuity in pressure across the interface.

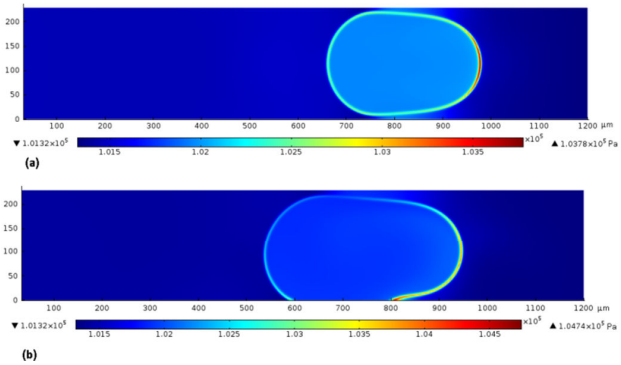

Fig. 6 The pressure distributions of the central XY plane (a) and the central ZY plane (b) at t = 1.8 ms

ACKNOWLEDGMENT

This project is supported by the Scientific and Technological Research Council of Turkey (TÜBİTAK) under grant number 112M168.

REFERENCES

[1] B. Agostini, M. Fabbri, J.E. Park, L. Wojtan, J.R. Thome, B. Michel, "State of the art of high heat flux cooling technologies," Heat Transfer Eng. 28, 2007, pp. 258–281.
[2] Z. Dong, J. Xu, F. Jiang, P. Liu, "Numerical study of vapor bubble effect on flow and heat transfer in microchannel," Int. J. Therm. Sci. 54, 2012, pp. 22-32.
[3] D.L. Sun, J.L. Xu, L. Wang, "Development of a vapor-liquid phase change model for volume-of-fluid method in FLUENT," Int. Comm. Heat Mass Transf. 39, 2012, pp.1101-1106.
[4] M. Magnini, B. Pulvirenti, J.R. Thome, "Numerical investigation of hydrodynamics and heat transfer of elongated bubbles during flow boiling in a microchannel," Int. J. Heat Mass transfer 59, 2013, pp. 451-471.
[5] L. Consolini, J.R. Thome, "A heat transfer model for evaporation of coalescing bubbles in micro-channel flow," Int. J. Heat Mass Transfer 31, 2010, pp. 115-125.
[6] A. Mukherjee, S.G. Kandlikar, Z.J. Edel, "Numerical study of bubble growth and wall heat transfer during flow boiling in a microchannel," Int. J. Heat Mass Transfer 54, 2011, pp. 3702-3718.
[7] P. Yue, C. Zhou, J.J. Feng, C.F. Ollivier-Gooch, H.H. Hu, "Phase-field simulations of interfacial dynamics in viscoelastic fluids using finite elements with adaptive meshing," J. Comput. Phys. 219, 2006, pp. 47–67.
[8] D.M. Anderson, G.B. McFadden, "Diffuse-interface methods in fluid mechanics," Annu. Rev. Fluid Mech. 30, 1998, pp. 139–165.

[9] C. Liu, J. Shen, "A phase-field model for the mixture of two incompressible fluids and its approximation by a Fourier-spectral method," Physica D 179, 2003, pp. 211–228.
[10] P. Yue, J.J. Feng, C. Liu, J. Shen, "A diffuse-interface method for simulating two-phase flows of complex fluids," J. Fluid Mech. 515, 2004, pp. 293–317.
[11] W. Lee, G. Son, "Bubble Dynamics and Heat Transfer during Nucleate Boiling in a Microchannel," Numerical Heat Transfer, Part A 53, 2008, pp. 1074–1090.
[12] H. Gomez, V.M. Calo, Y. Bazilevs, T. J.R. Hughes, "Isogeometric analysis of the Cahn-Hilliard phase-field model," Comput. Methods Appl. Mech. Engrg. 197, 2008, pp. 4333–4352.
[13] I. Steinbach, "Phase-field models in materials science," Modelling Simul. Mater. Sci. Eng. 17, 2009, pp. 073001-1-31.
[14] C. Miehe, F. Welschinger, M. Hofacker, "Thermodynamically consistent phase-field models of fracture: variational principles and multi-field FE implementations," Int. J. Numer. Meth. Engng 83, 2010, pp. 1273–1311.
[15] D. Jacqmin, "Calculation of two-phase Navier–Stokes flows using phase-field modeling," J. Comput. Phys. 155, 1999, pp. 96–127.
[16] H. D. Ceniceros, R. L. Nós, A. M. Romac, "Three-dimensional, fully adaptive simulations of phase-field fluid models," J. Comput. Phys. 229 , 2010, pp. 6135–6155.
[17] V.E. Badalassi, H.D. Ceniceros, S. Banerjee, "Computation of multiphase systems with phase field models," J. Comput. Phys. 190 , 2003, pp. 371–397.
[18] A. Badillo, "Quantitative phase-field modeling for boiling phenomena", Phys. Rev. E 86, 2012, pp. 041603-1-25.
[19] W.H. Lee, "A pressure iteration scheme for two-phase flow modeling," T.N. Veziroglu (Ed.), Multiphase Transport Fundamentals, Reactor Safety, Applications, vol. 1, Hemisphere Publishing, Washington, DC, 1980.